Geochemical Perspectives Letters

$Fe(II)_{aq}$-induced transformation of Fe-rich precipitates from a hydrothermal field

Z. Zhou[1], J. Li[1*], L. Notini[2], Z. He[1], M. Schad[3], K.O. Konhauser[3], S. Yang[1]

https://doi.org/10.7185/geochemlet.2531

Abstract

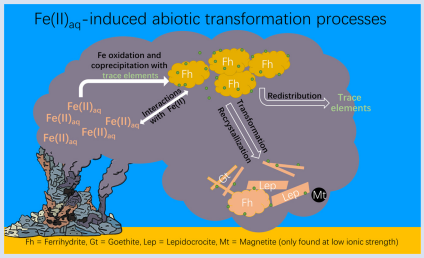

Aqueous ferrous iron ($Fe(II)_{aq}$) is known to induce recrystallisation of Fe(III) oxyhydroxides, yet the relevance and implications of this process in low temperature hydrothermal systems remain underexplored. In this study, we investigated natural Fe-rich precipitates containing mixed phases (ferrihydrite, goethite, lepidocrocite) collected from the Longqi Hydrothermal Field on the Southwest Indian Ridge. These precipitates were then incubated with ^{57}Fe labeled $Fe(II)_{aq}$ under anoxic laboratory conditions. Our results show that $Fe(II)_{aq}$ induced rapid mineral transformation of the Fe-rich precipitates containing the geochemical and mineralogical complexity of hydrothermal systems. Secondary lepidocrocite and goethite formed readily, and magnetite was observed under conditions with a high solid Fe(II)/Fe(III) ratio. The $^{57}Fe(II)$ tracer revealed rapid Fe atom exchange between $Fe(II)_{aq}$ and structural Fe(III) (*e.g.*, pre-existing goethite), leading to increased crystallinity. During the prompt and extensive Fe(II)-induced mineral transformation and recrystallisation, we also identified the development of new morphological features (*e.g.*, lath-like structures) on mineral surfaces, alongside the redistribution of associated Co, Ni, Cu, Zn, and Ba. This suggests their enhanced mobility and potential fluxes to surrounding seawater. Together, these results provide essential, yet frequently overlooked, insights into the role of Fe(II)-Fe(III) interactions in shaping both mineralogical evolution and trace element cycling within Fe-rich hydrothermal systems.

Received 11 May 2025 | Accepted 23 July 2025 | Published 3 September 2025

Introduction

Iron and other trace elements released from hydrothermal vents are critical contributors to marine biogeochemical cycles (Elderfield and Schultz, 1996; Resing *et al.*, 2015). In low temperature hydrothermal systems, the mixing of Fe-rich fluids with oxygenated seawater, combined with biomineralisation by Fe(II)-oxidising bacteria, triggers rapid precipitation of amorphous and poorly crystalline Fe(III) oxyhydroxides (*e.g.*, ferrihydrite). These metastable phases act as transient sinks for trace elements and nutrients, such as cobalt (Co), nickel (Ni), silicon (Si), and phosphorus (P), thereby regulating their fluxes into surrounding seawater (German *et al.*, 1991). Yet, these initially formed Fe(III) oxyhydroxides undergo transformations during deposition and burial, with important implications for the mobility and fate of associated trace elements. While microbial mediated mineralisation processes in these setting have been relatively well studied (Konhauser and Riding, 2012), the role of $Fe(II)_{aq}$ — which is ubiquitous in hydrothermal fluids and porewaters — in driving subsequent mineral transformation remains poorly constrained within hydrothermal systems.

Fe(II)-induced transformation of Fe(III) oxyhydroxides is well documented in laboratory experiments using synthetic Fe minerals such as ferrihydrite and lepidocrocite (Liu *et al.*, 2022; Hua *et al.*, 2023). Extensive Fe atom exchange between $Fe(II)_{aq}$ and structural Fe(III) has also been identified even without noticeable mineral transformation (Handler *et al.*, 2014; Chen *et al.*, 2023). This Fe(II)-induced "cryptic" recrystallisation and transformation not only alters the mineralogy of Fe(III) oxyhydroxides, but also affects the stability of associated trace metals (Frierdich *et al.*, 2011; Hua *et al.*, 2023). Additionally, it can drive Fe isotope fractionation among different mineral phases, complicating the interpretation of Fe isotope signatures to trace the origin and formation of Fe deposits (Johnson *et al.*, 2020; Fitzsimmons and Conway, 2023). However, natural hydrothermal systems are a unique matrix of mineralogical and geochemical environments, with major and trace elemental compositions that may impede or redirect the transformation pathways of Fe-rich precipitates (Jones *et al.*, 2009; Li *et al.*, 2024). Studies relying solely on laboratory synthesised minerals may therefore fail to capture the full range of processes occurring *in situ*, underscoring the need to investigate $Fe(II)_{aq}$-induced processes using geochemically realistic samples from actual hydrothermal systems.

In this study, we address this knowledge gap by studying natural Fe-rich precipitates collected from the Longqi Hydrothermal Field on the Southwest Indian Ridge. These samples preserve the chemical and mineralogical complexity of natural systems, allowing us to explore $Fe(II)_{aq}$-induced processes under environmentally relevant conditions. By coupling $^{57}Fe(II)$ stable isotope tracer experiments with mass spectroscopy,

1. State Key Laboratory of Marine Geology, Tongji University, Shanghai, China
2. Department of Civil, Construction, and Environmental Engineering, University of Delaware, Newark, DE, USA
3. Department of Earth and Atmospheric Sciences, University of Alberta, Edmonton, AB, Canada
* Corresponding author (email: jtli@tongji.edu.cn)

scanning and transmission electron microscopy, X-ray diffraction, and Mössbauer spectroscopy, we tracked mineralogical and morphological changes in detail and identified Fe atom exchange and trace metal redistribution in laboratory conditions. Our findings highlight the often overlooked role of $Fe(II)_{aq}$ in modern low temperature hydrothermal systems in addition to biomineralisation, providing additional constraints for interpreting sedimentary records in modern and ancient Fe deposits.

Materials and Methods

Sample collection. Fe-rich precipitates were sampled from the Longqi low temperature hydrothermal field on the Southwest Indian Ridge, near an active vent located at 49.6497° E, 37.7832° S, at a water depth of ~2750 metres (Fig. 1). Ambient water temperatures ranged from 50–60 °C near the vent to 2–4 °C farther away, with pH values between 7.8–8.0. Sampling was carried out December 2, 2018, using the RV Tansuoyihao and the submersible "Shenghaiyongshi". Immediately upon retrieval, the precipitate suspension (solid-liquid ratio was about 1:1) was preserved at −80 °C until further processing. Prior to commencing our experiments, an aliquot of the precipitate suspension was totally digested by 6 M HCl to determine the concentrations of Fe and other elements in the stock (see Table S-1).

Experiments. All experiments were conducted inside an anoxic glovebox under N_2 atmosphere ($O_2 < 0.2$ ppm). Ultrapure water was deoxygenated by purging with N_2 and equilibrated within the glovebox for one week before preparing anoxic solutions. A stock solution of $^{57}Fe(II)$ was prepared by dissolving metallic ^{57}Fe (96 % of ^{57}Fe, ISOFLEX, California) in 1 M HCl (double distilled). This solution was then used to obtain 2 mM $^{57}Fe(II)$ in either HEPES buffer (25 mM, pH 8.0) or artificial seawater (ASW, pH 8.0, ionic strength 0.72 mol/L)(Kester *et al.*, 1967), and subsequently exposed to the Fe-rich precipitates (containing 10 mM Fe). Control experiments were performed with only $^{57}Fe(II)_{aq}$ or only the precipitates in HEPES buffer and ASW, respectively. For the reaction medium, HEPES buffer was used to isolate Fe(II) driven processes under controlled conditions and investigate their mechanistic feasibility, whereas ASW provided a more environmentally relevant context simulating hydrothermal systems. Although we acknowledge that the experimental setups cannot fully replicate natural conditions, key parameters such as pH (8.0) and Fe(II)/Fe(III) ratios were chosen to reflect conditions relevant to low temperature hydrothermal systems.

Triplicate reactors were rotated in the dark and sampled over a 14 day reaction period. Aliquots were centrifuged, and the resulting solids were subjected to sequential extractions: 1 M $MgCl_2$ to isolate the exchangeable fraction, 0.5 M HCl to target the amorphous to poorly crystalline Fe fraction, and 6 M HCl for the crystalline Fe fraction. More detailed methods can be found in SI. Aqueous trace metals (Co, Ni, Zn, Cu, and Ba) were quantified separately by ICP-MS, using ^{103}Rh and ^{115}In as

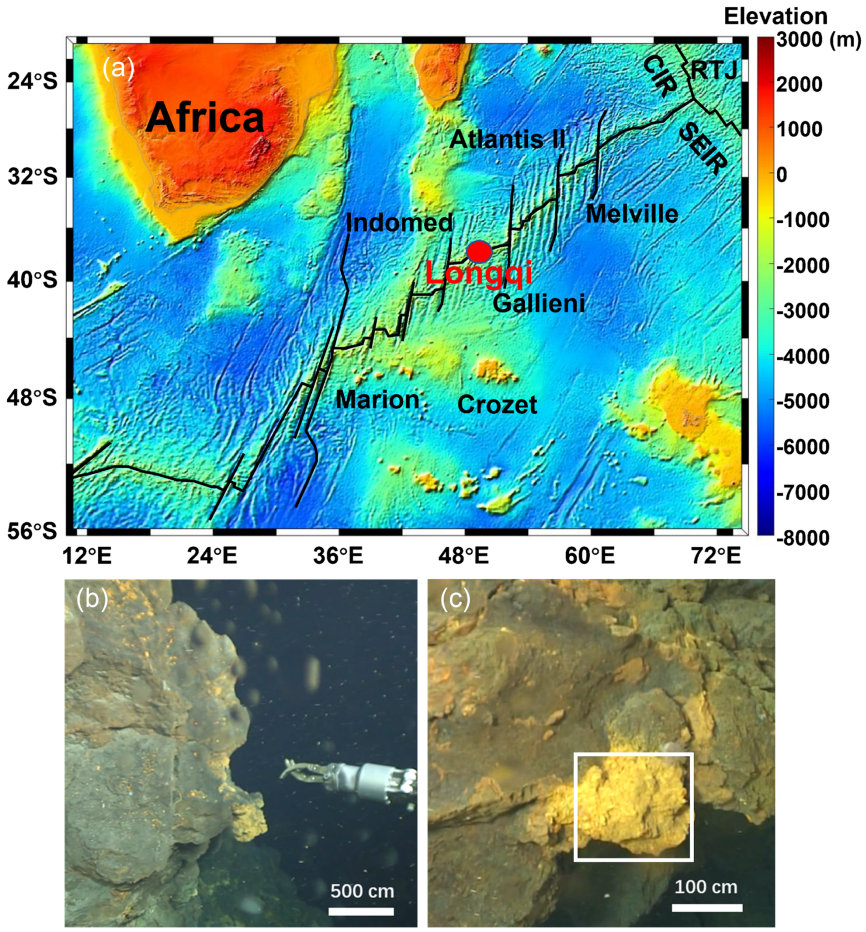

Figure 1 **(a)** The geotectonic setting and location of Longqi hydrothermal field. **(b)** Photo of sampling site that is away from active vent, and **(c)** the specific sampling point of the Fe-rich precipitates used in this study, with environmental pH (7.8–8.0) and temperature ranged from 50–60 °C (closer to vent) to 2–4 °C that is similar to ambient deep sea water.

internal standards. The count rate stability of the instrument was maintained below 3 % relative standard deviation (RSD).

Mineral characterisation. To track microstructural changes, aliquots of sediment suspensions were placed on a copper observation table and a copper net, dried in an anoxic glovebox, and characterised with a field emission scanning electron microscope (SEM Nano 450, FEI Co., USA) and a transmission electron microscope (TEM, JEOL JEM-F200, Japan). Due to limited sample volumes, unreacted and reacted samples were filtered (0.22 μm) and characterised using micro X-ray diffraction (μXRD, Bruker D8 Endeavor, Germany). The ^{57}Fe Mössbauer Spectroscopy (Wissel GmbH, Germany) was also applied to track the mineralogical changes. More detailed methods about mineral characterisation can be found in the Supplementary Information.

Results and Discussion

Characteristics of the hydrothermal Fe-rich precipitates. The Fe-rich precipitates investigated in this study primarily consist of amorphous to poorly crystalline Fe(III) phases (*e.g.*, ferrihydrite), goethite, and lepidocrocite, as identified by HCl extractions (Fig. 2), TEM imaging (Fig. 3), XRD, and Mössbauer spectroscopy (Fig. 4). Approximately 25 % of Fe in the original precipitates was extractable with 0.5 M HCl, and 100 % was extractable with 6 M HCl, indicating the relatively low stability of these Fe(III) oxyhydroxides (Fig. 2). Morphologically, both amorphous and rod-like hollow structures were observed (Fig. 3a1,a2), suggesting that abiotic and microbially mediated Fe(II) oxidation both contributed to their formation (Chan *et al.*, 2016; Li *et al.*, 2024). EDS analysis showed a very low abundance of Si (< 1%) within these structures (Fig. S-1). The crystallinity and structural order of these minerals were further elucidated by selected area electron diffraction (SAED) associated with TEM (Fig. 3a5), the full width at half maximum (FWHM) of identical peaks in XRD patterns (Table S-2), and magnetic ordering from ^{57}Fe Mössbauer spectra at 295 K (Fig. 4b). Collectively, these analyses reveal structural defects in the crystal structures, particularly in goethite with the nanoneedle morphology. Notably, the relatively high proportion of crystallised Fe minerals (goethite and lepidocrocite) combined with low Si content (< 1 %; Fig. S-1) distinguishes these precipitates from those described in our previous study, where only poorly crystalline Fe(III) oxyhydroxides, such as ferrihydrite, were identified (Li *et al.*, 2024).

Reactions with Fe(II). While microbial mediated mineral formation and transformation are crucial, this study intentionally focuses on abiotic processes mediated by $Fe(II)_{aq}$, which are comparatively understudied in hydrothermal systems. By reacting Fe-rich precipitates with $Fe(II)_{aq}$ at an initial Fe(II)/Fe(III) ratio of 0.2, 91 % of $Fe(II)_{aq}$ was removed over 14 days in the HEPES buffer, resulting in a final Fe(II)/Fe(III) ratio of 0.14 in the solid phase (Fig. 2a). Sequential extraction revealed a significant decrease in the total Fe content within the 0.5 M HCl

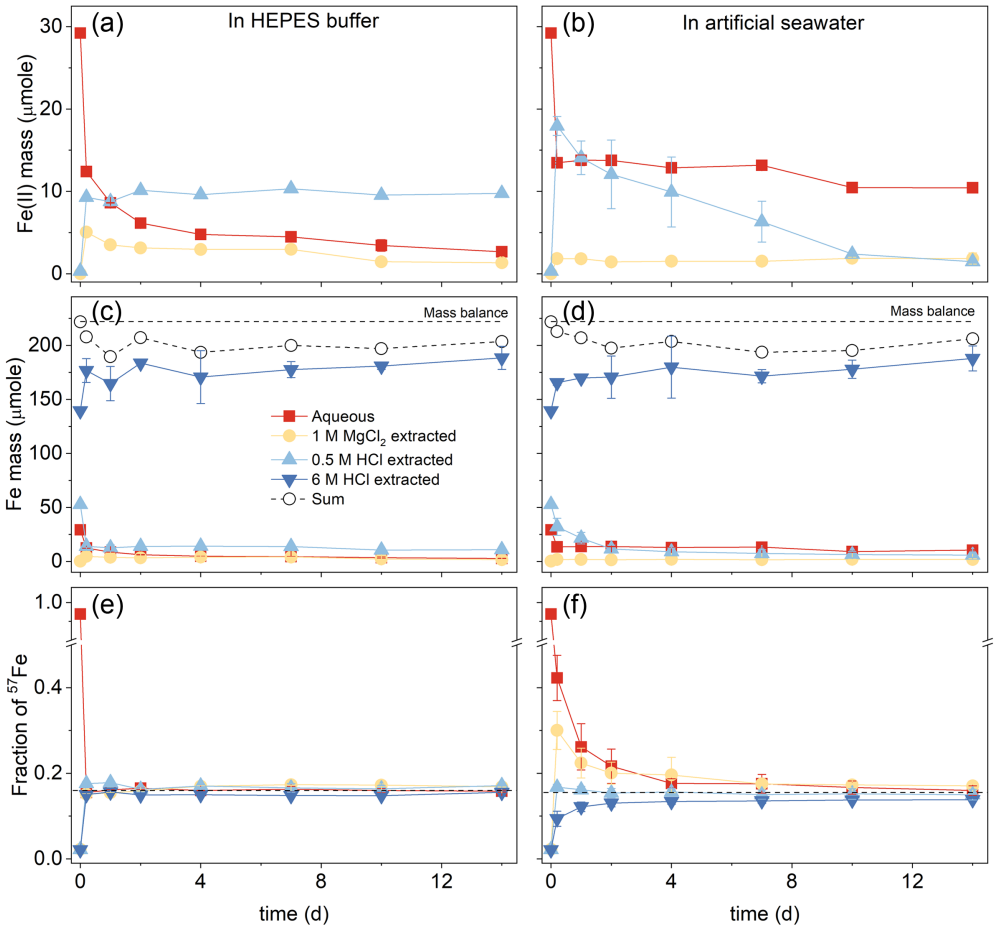

Figure 2 The mass of Fe(II) **(a, b)** and total Fe **(c, d),** as well as the fraction of ^{57}Fe in the aqueous, exchangeable (1 M $MgCl_2$ extracted), and 0.5 M HCl extracted pools during the reaction in HEPES buffer **(a, c, e)** or artificial seawater **(b, d, f).** The dashed lines in **(c)-(f)** represent the mass or isotope balance. The overall Fe recovery rate was 91 ± 3 %. Each point represents the mean ± standard deviation of triplicate reactors. Where error bars are not visible, they are smaller than the symbols.

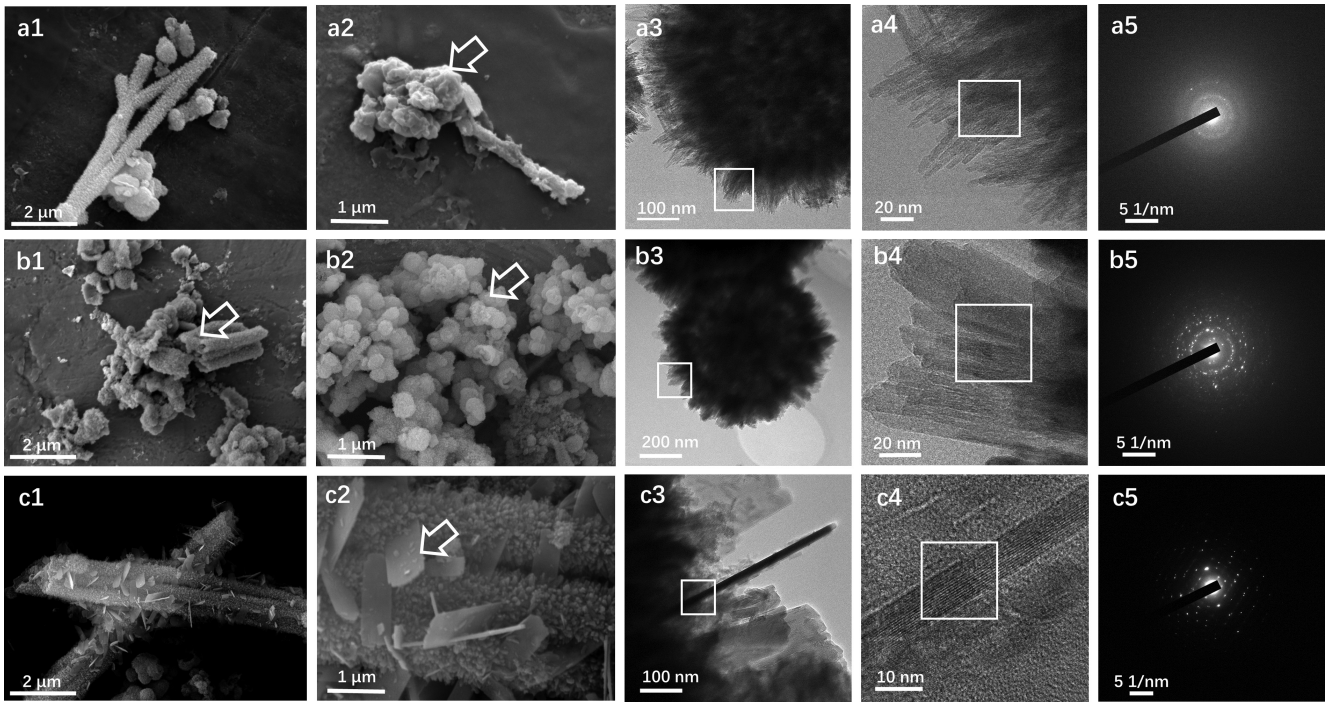

Figure 3 Images of typical mineral structures in the Fe-rich precipitates of the control group **(a)**, treated with Fe(II) in HEPES buffer **(b)**, and in artificial seawater **(c)**. Columns 1 and 2 represent SEM images, 3 and 4 represent TEM images, and 5 represents the images of SAED. Arrows point to the specific feature discussed in the text. Squared area represents the focus of the following image.

extractable fraction, accompanied by an increase in the 6 M HCl extractable fraction, indicating a shift towards more stable and crystalline mineral phases. Rapid Fe isotope mixing was identified, with the fraction of ^{57}Fe in different phases reaching near equilibrium (^{57}Fe fraction ~0.16) within two days (Fig. 2e). Visually, the solid phase exhibited a noticeable colour change from yellowish to blackish, signaling substantial mineralogical transformation.

In ASW, the removal of Fe(II)$_{aq}$ proceeded more slowly, with only 50 % removed over 14 days, resulting in a final Fe (II)/Fe(III) ratio of 0.09 in the solid phase (Fig. 2b). This slower removal is mainly due to cation competition with Fe(II) for adsorption sites at high ionic strength. Correspondingly, both the Fe(II) and total Fe mass in the 0.5 M HCl extractable fraction decreased more gradually, and Fe isotope exchange proceeded at a slower rate compared to the reaction in HEPES buffer (Fig. 2d, f), mainly due to the lower Fe(II) loading in the solid phase. Although no visible colour change was observed as seen under the HEPES buffered conditions, microstructural alterations in the solid phase were nevertheless evident in both SEM and TEM analyses.

Morphological and mineralogical alterations. Compared to the control group containing only the original precipitates, the long rod-like hollow structures were generally shorter and showed signs of fragmentation after reaction with Fe(II)$_{aq}$ in HEPES buffer (Fig. 3a1,b1). Additionally, new spherical particle agglomerates formed, indicating substantial mineral transformation likely driven by Fe(II)$_{aq}$ (Fig. 3b2). In ASW, the rod-like hollow structure and nanoneedles were largely preserved, although an additional lath-shaped structure appeared, indicating significant modifications to the morphological features (Fig. 3c1,c2).

TEM, XRD and Mössbauer spectroscopy provided further insights into these transformations. After reaction with Fe(II)$_{aq}$ in HEPES buffer, the abundance of non-crystalline phases in the original precipitates was diminished, corresponding to the formation of more crystallised Fe minerals (Fig. 4). In the XRD pattern, magnetite identical peaks appeared, consistent with the spherical particles observed in SEM images (Figs. 4a, 3b2). In contrast, a higher proportion of non-crystalline phases persisted in ASW (Fig. 4e, Table S-3), accompanied by the formation of secondary goethite and lepidocrocite (Fig. 4a). The ratio of lepidocrocite to goethite decreased from 0.45 to 0.31 after reaction with Fe(II)$_{aq}$, indicating the enrichment of goethite after mineralogical transformation.

Comparing the SAED of the nanoneedles (Fig. 3) and the FWHM values of the goethite [110] face (Table S-2), we observed an improvement in goethite crystallinity after reaction with Fe (II)$_{aq}$ in both media. This observation is linked to extensive Fe atom exchange between Fe(II)$_{aq}$ and structural Fe(III) within the crystalline Fe minerals (corresponding to the 6 M HCl extractable; Fig. 2e,f). These results suggest that Fe(II)-induced recrystallisation of goethite occurred, leading to a reduction in crystal defects by removing site vacancy or substitutions (Notini *et al.*, 2018; Southall *et al.*, 2018). The increased concentration of trace metals immediately after reaction with Fe(II)$_{aq}$ (Fig. S-4) also supports this interpretation (Frierdich *et al.*, 2011).

Conversely, in ASW which better simulates natural conditions, the crystallinity of lepidocrocite decreased (Table S-2). This reduction in crystallinity may result from transformation of pre-existing lepidocrocite into secondary goethite, with the pre-existing goethite potentially serving as a template (Yin *et al.*, 2025). Additionally, the identified lepidocrocite could be newly formed, promoted by the "lepidocrocite favouring effect" during ferrihydrite transformation influenced by natural components (Chen *et al.*, 2015). The relatively short aging time of this secondary lepidocrocite likely accounts for its lower crystallinity. This interpretation is also supported by the emergence of newly formed lath-shaped structures (Fig. 3c1,c2). Overall, our findings based on laboratory experiments provide direct evidence that Fe(II)$_{aq}$ can induce rapid mineral transformation and

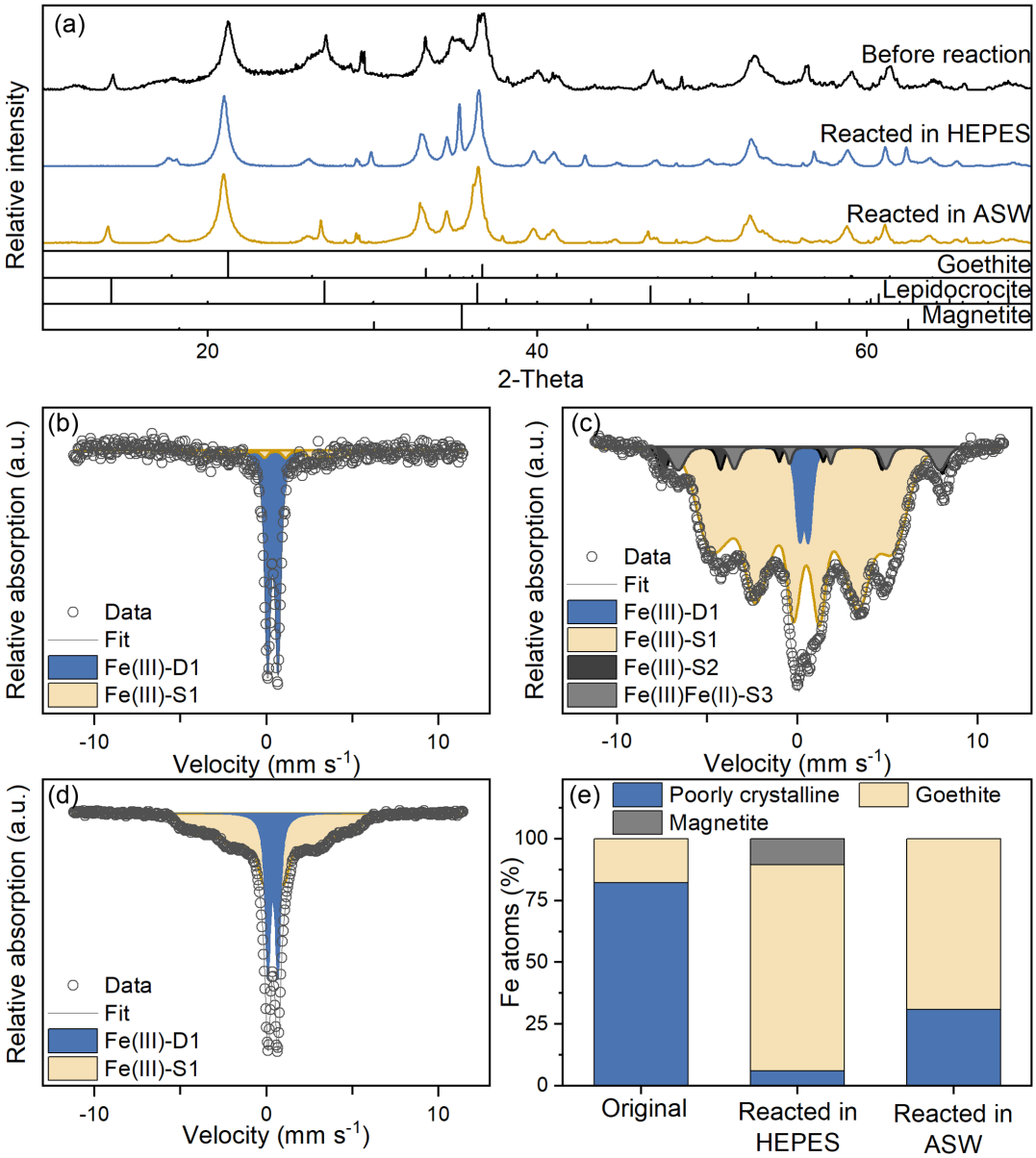

Figure 4 **(a)** X-ray diffraction patterns of Fe-rich precipitates before and after reaction with $Fe(II)_{aq}$ in HEPES buffer and artificial seawater; Mössbauer spectra of Fe-rich precipitates **(b)** before reaction; **(c)** reacted in HEPES buffer; and **(d)** reacted in artificial seawater. The spectra were collected at 295 K. **(e)** The estimated percent of Fe atoms in each phase based on Mössbauer spectrum and XRD patterns. Please note the Mössbauer spectra of poorly crystalline minerals (*e.g.*, ferrihydrite, lepidocrocite) are difficult to resolve at room temperature, and a mixed phase of Fe(III)-D1 was introduced to constrain them.

recrystallisation within Fe-rich precipitates derived from the low temperature hydrothermal systems.

Coupled trace element cycling. During Fe(II)-induced mineral transformation and recrystallisation, we observed a rapid release of Ni, Co, Cu, Zn and Ba at the beginning of the reactions, followed by near complete resorption of Ni within one day (Figs. S-3, S-4). The concentrations of Co, Cu, Zn and Ba were significantly higher in ASW compared to the HEPES buffer, likely due to higher background levels and cation desorption driven by the higher ionic strength of ASW (Fig. S-3). Most of the trace metal release occurred immediately after $Fe(II)_{aq}$ adsorption, which could be attributed to cation exchange with $Fe(II)_{aq}$ and a reduction in available binding sites within the newly formed secondary minerals (Liu *et al.*, 2016). Importantly, this prompt Fe(II)-induced release of trace elements is crucial for their remobilisation, potentially allowing them to escape capture by Fe(III) oxyhydroxides within the hydrothermal plume (Lough, 2016). In natural environments, dynamic mixing of hydrothermal fluids with surrounding seawater further facilitates the efficient export of these remobilised trace elements, potentially enhancing their fluxes from hydrothermal systems to the ocean.

Implications for the Fe-rich precipitates formation processes. A number of studies have highlighted the role of Fe(II)-oxidising microorganisms in forming Fe-rich precipitates and characteristic morphological features in low temperature hydrothermal fields (Konhauser *et al.*, 2017; Dong *et al.*, 2022; Li *et al.*, 2024). Complementing this microbial perspective, our study underscores the importance of $Fe(II)_{aq}$ in driving subsequent transformation and recrystallisation of Fe-rich precipitates in these environments.

Our experimental findings, together with previous studies, demonstrate that secondary minerals such as goethite,

magnetite, and some intermediate minerals (*e.g.*, lepidocrocite, green rust) can form rapidly when settling Fe(III) oxyhydroxides interact with $Fe(II)_{aq}$ within a hydrothermal plume or during the hydrothermal alteration of Fe deposits (Zegeye *et al.*, 2012; Li *et al.*, 2017). While our experimental setup may not fully replicate all conditions of the natural environment, especially the system with HEPES buffer, the high Fe(II)/Fe(III) ratios achieved in the solid phase, a key factor for magnetite formation (Bauer *et al.*, 2020), is plausible within a hydrothermal plume or during post-depositional processes, such as those proposed for Precambrian hydrothermal systems (Kump and Seyfried, 2005). These results suggest that Fe(II)-induced magnetite formation can occur not only in high temperature settings (Li *et al.*, 2017) but also in low temperature hydrothermal systems. Furthermore, the secondary lath-shaped structures identified in our experiments closely resemble those observed in natural hydrothermal deposits (Li *et al.*, 2024), implying that such morphologies could serve as indicators for Fe(II)-induced mineral transformation under anoxic and Fe(II)-rich ("ferruginous") conditions.

Additionally, the $^{57}Fe(II)$ tracer experiments revealed rapid Fe atom exchange between $Fe(II)_{aq}$ and the ferric substrates of varying crystallinity (Fig 2e,f). The prevalence of crystal defects in naturally occuring minerals likely facilitated this efficient Fe atom exchange (Notini *et al.*, 2018), enabling the Fe(II)-induced recrystallisation to play a part even in limited coexistence time of $Fe(II)_{aq}$ and Fe(III) oxyhydroxides in the hydrothermal plume. This rapid Fe atom exchange also suggests an additional mechanism of Fe isotope fractionation, thus posing potential constraints on the interpretation of Fe isotope signals in hydrothermal systems (Johnson *et al.*, 2020). Furthermore, the concurrent redistribution of associated trace elements during mineral transformation and recrystallisation may promote their release into surrounding seawater (Frierdich *et al.*, 2011; Liu *et al.*, 2016; Gini *et al.*, 2024). Taken together, these findings highlight the need to take into account Fe(II)-induced processes when reconstructing geochemical cycling and the formation pathways for Fe-rich precipitates. More complex experimental setups better simulating natural conditions and covering greater geochemical gradients will be needed to further elucidate the implications of Fe(II)-Fe(III) interactions in the hydrothermal system.

Drawing parallels between modern hydrothermal systems and the depositional environments of ancient iron formations (IFs), our findings suggest that in addition to biomineralisation processes, the abiotic Fe(II)-induced processes could have also played a role in iron deposition on early Earth. During the Great Oxidation Event (GOE), redox stratification within the ocean water column may have permitted the coexistence of $Fe(II)_{aq}$ and Fe(III) oxyhydroxides over a broad spatial and temporal scale (Zegeye *et al.*, 2012; Liang *et al.*, 2025). Consequently, Fe(II)-induced mineral transformation of settling Fe(III) oxyhydroxides and concurrent recrystallisation could have enhanced the crystallinity of Fe minerals and fractionated Fe isotope compositions in IFs (Johnson *et al.*, 2020). Furthermore, Fe(II)-induced processes may have facilitated the release of micronutrients (*e.g.*, Co, Ni, Cu, Zn) from amorphous to poorly crystalline Fe(III) oxyhydroxides formed during oxygenation, thus increasing nutrient availability for early marine microorganisms in ancient oceans.

Acknowledgements

Financial support was provided by the National Key Research and Development Program of China (2021YFF0501301), the National Science Foundation of China (42306052; 42230410; 42072333), and the Shanghai Pilot Program for Basic Research. We thank Shanghai Synchrotron Radiation Facility for the beam time granted under project NO.2024-SSRF-PT-510157. We thank Prof. Hu Wang, Dr. Lei Su, Yan Zhang and Yue Sheng for their help with sample preparations and background information. We would also like to acknowledge all the reviewers and editors for their constructive comments which significantly improved the quality of this work.

Editor: Juan Liu

Additional Information

Supplementary Information accompanies this letter at https://www.geochemicalperspectivesletters.org/article2531.

Cite this letter as: Zhou, Z., Li, J., Notini, L., He, Z., Schad, M., Konhauser, K.O., Yang, S. (2025) $Fe(II)_{aq}$-induced transformation of Fe-rich precipitates from a hydrothermal field. *Geochem. Persp. Let.* 36, 28–34. https://doi.org/10.7185/geochemlet.2531

References

Bauer, K., Byrne, J., Kenward, P., Simister, R., Michiels, C., Friese, A., Vuillemin, A., Henny, C., Nomosatryo, S., Kallmeyer, J. (2020) Magnetite biomineralization in ferruginous waters and early Earth evolution. *Earth and Planetary Science Letters* 549, 116495. https://doi.org/10.1016/j.epsl.2020.116495

Chan, C.S., McAllister, S.M., Leavitt, A.H., Glazer, B.T., Krepski, S.T., Emerson, D. (2016) The Architecture of Iron Microbial Mats Reflects the Adaptation of Chemolithotrophic Iron Oxidation in Freshwater and Marine Environments. *Frontiers in Microbiology* 7, 796. https://doi.org/10.3389/fmicb.2016.00796

Chen, C., Dong, Y., Thompson, A. (2023) Electron Transfer, Atom Exchange, and Transformation of Iron Minerals in Soils: The Influence of Soil Organic Matter. *Environmental Science and Technology* 57, 10696–10707. https://doi.org/10.1021/acs.est.3c01876

Chen, C., Kukkadapu, R., Sparks, D.L. (2015) Influence of coprecipitated organic matter on $Fe^{2+}_{(aq)}$-catalyzed transformation of ferrihydrite: implications for carbon dynamics. *Environmental Science and Technology* 49, 10927–10936. https://doi.org/10.1021/acs.est.5b02448

Dong, A., Sun, Z., Kendall, B., Izon, G., Cao, H., Li, Z., Ma, X., Yin, X., Qiu, Z., Zhu, X.-k., Bekker, A., Poulton, S.W. (2022) Insights from modern diffuse-flow hydrothermal systems into the origin of post-GOE deep-water Fe-Si precipitates. *Geochimica et Cosmochimica Acta* 317, 1–17. https://doi.org/10.1016/j.gca.2021.10.001

Elderfield, H., Schultz, A. (1996) Mid-Ocean Ridge Hydrothermal Fluxes and the Chemical Composition of the Ocean. *Annual Review of Earth and Planetary Sciences* 24, 191–224. https://doi.org/10.1146/annurev.earth.24.1.191

Fitzsimmons, J.N., Conway, T.M. (2023) Novel Insights into Marine Iron Biogeochemistry from Iron Isotopes. *Annual Review of Marine Science* 15, 383–406. https://doi.org/10.1146/annurev-marine-032822-103431

Frierdich, A.J., Luo, Y., Catalano, J.G. (2011) Trace element cycling through iron oxide minerals during redox-driven dynamic recrystallization. *Geology* 39, 1083–1086. https://doi.org/10.1130/G32330.1

German, C.R., Campbell, A.C., Edmond, J.M. (1991) Hydrothermal scavenging at the Mid-Atlantic Ridge: Modification of trace element dissolved fluxes. *Earth and Planetary Science Letters* 107, 101–114. https://doi.org/10.1016/0012-821X(91)90047-L

Gini, C., Jamieson, J.W., Reeves, E.P., Gartman, A., Barreyre, T., Babechuk, M.G., Jørgensen, S.L., Robert, K. (2024) Iron Oxyhydroxide-Rich

Hydrothermal Deposits at the High-Temperature Fåvne Vent Field, Mohns Ridge. *Geochemistry, Geophysics, Geosystems* 25, e2024GC011481. https://doi.org/10.1029/2024GC011481

Handler, R.M., Frierdich, A.J., Johnson, C.M., Rosso, K.M., Beard, B.L., Wang, C.M., Latta, D.E., Neumann, A., Pasakarnis, T., Premaratne, W., Scherer, M.M. (2014) Fe(II)-Catalyzed Recrystallization of Goethite Revisited. *Environmental Science and Technology* 48, 11302–11311. https://doi.org/10.1021/es503084u

Hua, J., Sun, J., Chen, M., Liu, C., Wu, F. (2023) Aqueous Fe(II)-catalyzed iron oxide recrystallization: Fe redox cycling and atom exchange, mineralogical recrystallization and contributing factor. *Reviews in Environmental Science and Bio/Technology* 22, 55–78. https://doi.org/10.1007/s11157-023-09646-3

Johnson, C., Beard, B., Weyer, S. (2020) *Iron Geochemistry: An Isotopic Perspective*. Springer, Cham. https://doi.org/10.1007/978-3-030-33828-2

Jones, A.M., Collins, R.N., Rose, J., Waite, T.D. (2009) The effect of silica and natural organic matter on the Fe(II)-catalysed transformation and reactivity of Fe(III) minerals. *Geochimica et Cosmochimica Acta* 73, 4409–4422. https://doi.org/10.1016/j.gca.2009.04.025

Kester, D.R., Duedall, I.W., Connors, D.N., Pytkowicz, R.M. (1967) Preparation of artificial Seawater. *Limnology and Oceanography* 12, 176–179. https://doi.org/10.4319/lo.1967.12.1.0176

Konhauser, K.O., Riding, R. (2012) Bacterial Biomineralization. In: Knoll, A.H., Canfield, D.E., Konhauser, K.O. (Eds.) *Fundamentals of Geobiology*. Wiley-Blackwell, Oxford, 105–130. https://doi.org/10.1002/9781118280874.ch8

Konhauser, K.O., Planavsky, N.J., Hardisty, D.S., Robbins, L.J., Warchola, T.J., Haugaard, R., Lalonde, S.V., Partin, C.A., Oonk, P.B.H., Tsikos, H., Lyons, T.W., Bekker, A., Johnson, C.M. (2017) Iron formations: A global record of Neoarchaean to Palaeoproterozoic environmental history. *Earth-Science Reviews* 172, 140–177. https://doi.org/10.1016/j.earscirev.2017.06.012

Kump, L.R., Seyfried, W.E. (2005) Hydrothermal Fe fluxes during the Precambrian: Effect of low oceanic sulfate concentrations and low hydrostatic pressure on the composition of black smokers. *Earth and Planetary Science Letters* 235, 654–662. https://doi.org/10.1016/j.epsl.2005.04.040

Li, J., Sun, M., Qi, W., Zhou, Z., Hohl, S.V., He, Z. (2024) Geochemical and Sr-Nd-Pb-Fe Isotopic Constraints on the Formation of Fe-Si Oxyhydroxide Deposits at the Ultraslow-Spreading Southwest Indian Ridge. *Geochemistry, Geophysics, Geosystems* 25, e2023GC011185. https://doi.org/10.1029/2023GC011185

Li, Y.-L., Konhauser, K.O., Zhai, M. (2017) The formation of magnetite in the early Archean oceans. *Earth and Planetary Science Letters* 466, 103–114. https://doi.org/10.1016/j.epsl.2017.03.013

Liang, X., Stüeken, E.E., Alessi, D.S., Konhauser, K.O., Li, L. (2025) A seawater oxygen oscillation recorded by iron formations prior to the Great Oxidation Event. *Nature Geoscience* 18, 417–422. https://doi.org/10.1038/s41561-025-01683-7

Liu, C., Zhu, Z., Li, F., Liu, T., Liao, C., Lee, J.-J., Shih, K., Tao, L., Wu, Y. (2016) Fe(II)-induced phase transformation of ferrihydrite: The inhibition effects and stabilization of divalent metal cations. *Chemical Geology* 444, 110–119. https://doi.org/10.1016/j.chemgeo.2016.10.002

Liu, J., Sheng, A., Li, X., Arai, Y., Ding, Y., Nie, M., Yan, M., Rosso, K.M. (2022) Understanding the importance of labile Fe (III) during Fe (II)-catalyzed transformation of metastable iron oxyhydroxides. *Environmental Science and Technology* 56, 3801–3811. https://doi.org/10.1021/acs.est.1c08044

Lough, A.J.M. (2016) *Trace metal chemistry of hydrothermal plumes*. PhD Thesis, University of Southampton, *Ocean & Earth Science*. https://eprints.soton.ac.uk/403372/

Notini, L., Latta, D.E., Neumann, A., Pearce, C.I., Sassi, M., N'Diaye, A.T., Rosso, K.M., Scherer, M.M. (2018) The Role of Defects in Fe (II)–Goethite Electron Transfer. *Environmental Science and Technology* 52, 2751–2759. https://doi.org/10.1021/acs.est.7b05772

Resing, J.A., Sedwick, P.N., German, C.R., Jenkins, W.J., Moffett, J.W., Sohst, B.M., Tagliabue, A. (2015) Basin-scale transport of hydrothermal dissolved metals across the South Pacific Ocean. *Nature* 523, 200–203. https://doi.org/10.1038/nature14577

Southall, S.C., Mickletthwaite, S., Wilson, S., Frierdich, A.J. (2018) Changes in Crystallinity and Tracer-Isotope Distribution of Goethite during Fe(II)-Accelerated Recrystallization. *ACS Earth and Space Chemistry* 2, 1271–1282. https://doi.org/10.1021/acsearthspacechem.8b00100

Yin, M., Li, X., Guo, C., Zhong, Q., Li, X., Zeng, L., Zhou, Y., Yang, C., Dang, Z. (2025) Effects of coexisting goethite or lepidocrocite on Fe(II)-induced ferrihydrite transformation pathways and Cd speciation. *Science of the Total Environment* 959, 178321. https://doi.org/10.1016/j.scitotenv.2024.178321

Zegeye, A., Bonneville, S., Benning, L.G., Sturm, A., Fowle, D.A., Jones, C., Canfield, D.E., Ruby, C., MacLean, L.C., Nomosatryo, S., Crowe, S.A., Poulton, S.W. (2012) Green rust formation controls nutrient availability in a ferruginous water column. *Geology* 40, 599–602. https://doi.org/10.1130/G32959.1

Geochemical Perspectives Letters

$Fe(II)_{aq}$-induced transformation of Fe-rich precipitates from a hydrothermal field

Z. Zhou, J. Li, L. Notini, Z. He, M. Schad, K.O. Konhauser, S. Yang

Supplementary Information

The Supplementary Information includes:

- Supplementary Methods
- Tables S-1 to S-3
- Figures S-1 to S-4
- Supplementary Information References

Supplementary Methods

1. Sequential Fe Extractions

The extractions were conducted in a glovebox filled with N_2 (O_2 < 0.2 ppm). Triplicate reactors were sampled in regular intervals over 14 days of reaction. At each time point, aliquots were centrifuged, the supernatant filtered (0.22 µm) and subsequently acidified with HCl to preserve the Fe(II) in ~0.1 M HCl. The solids were subjected to sequential extractions under anoxic conditions using 1 M $MgCl_2$ (exchangeable Fe pool), 0.5 M HCl (amorphous to poorly crystalline Fe oxyhydroxides), and finally the residual solids were dissolved in 6 M HCl under microwave for 15 seconds (Voelz *et al.*, 2019). The concentrations of Fe(II) and total Fe in the aqueous, exchangeable, 0.5 M HCl extractable, and 6 M HCl extractable pools were analysed with a modified ferrozine method (Viollier *et al.*, 2000).

2. Fe Isotope Measurement

For Fe isotope composition, samples were diluted with 2% HNO_3 (double distilled) to achieve a final Fe concentration of ~2 µM, and analyzed using a quadrupole ICP-MS (Agilent 7900). He gas mode with a collision cell was applied to remove isobaric interferences with Argon (primarily $^{40}Ar^{16}O$ and $^{40}Ar^{16}O^{1}H$) for ^{56}Fe and ^{57}Fe (Zhou *et al.*, 2018). Four Fe isotopes (^{54}Fe, ^{56}Fe, ^{57}Fe, and ^{58}Fe) were measured, and the percent of ^{57}Fe in each sample was calculated as an indicator for Fe isotope mixing processes. Fe isotope standards (2.1 % and 96.0 % of ^{57}Fe) and internal standards of ^{103}Rh and ^{115}In were used to monitor instrument stability and correct between samples. The measurement precision of ^{57}Fe percent was about 0.1 %.

3. Mineral Characterization

For SEM, the samples were coated with Au and operated at 5–30 kV with a maximum beam current of 200nA. An energy dispersive X-ray spectrometer (EDS) was used to identify elemental compositions. The TEM was equipped with a Schottky gun operating at 200 kV (Cs 1.0 mm, Cc 1.1 mm, point resolution of 1.9 Å). XRD patterns were collected from 5-80° with a step increment of 0.02° (tube conditions: 40 kV, 40 mA; Cu source), and processed using MDI JADE 6.0. The relative peak intensities of lepidocrocite and goethite, as well as the full-width at half maximum (FWHM) of identical peaks, were analysis and verified by full-pattern fitting using Rietveld refinements. Samples were further analysed by 57Fe Mössbauer Spectroscopy (Wissel GmbH, Germany) at the East China Normal University. Mössbauer spectra were collected at 295 K using a 57Co source in a Rh lattice and calibrated against an α-Fe(0) foil. Spectral fitting was performed using the Recoil software (University of Ottawa, Canada) with an extended Voigt-Based fitting (xVBF) routine. The phase interpretations were based on established fitting parameters (Vandenberghe and De Grave, 2013).

Supplementary Tables

Table S-1 Major and trace element composition of the precipitate used in this study. The precipitate was digested by 6M HCl, which was strong enough to total dissolve the solid based on our pre-test.

Element	Na	Mg	Al	K	Ca	Fe	Li	Sc	Ti	V	Cr	Mn
			(%)						(ppm)			
Weight fraction	0.17	0.52	0.07	0.00	0.72	50.08	15.63	3.47	381.94	39.93	BDL*	BDL*

Element	Co	Ni	Cu	Zn	Ga	Rb	Sr	Mo	Cd	Ba	Nd	U
						(ppm)						
Weight fraction	24.31	13.89	2710.07	793.40	3.47	8.68	31.25	85.07	6.94	10.42	6.94	13.89

*Below detection limit.

Table S-2 The FWHM value of representative identical peaks in different samples.

Face	Full-width at half maximum (FWHM)		
	Control	Reacted in HEPES	Reacted in ASW
Goethite [110]	0.905	0.715	0.893
Lepidocrocite [200]	0.262	-	0.320

Table S-3 Fitting parameters for ^{57}Fe Mössbauer spectra of different samples.

Sample	Phase	Phase interpretation	Area %	Center shift (mm s^{-1})	QS or Ɛ [a] (mm s^{-1})	Hyperfine field (T)	σ[b] (mm s^{-1}) or (T)	Red-χ^2
Control	Fe(III)-D1	Paramagnetic Fe(III) phases, likely Fh, Lp and nGt	82.3	0.37	0.60	-	0.17	0.65
	Fe(III)-S1	Likely goethite	17.7	0.38	-0.12	24.00	4.00	
Reacted in HEPES	Fe(II)-D1	Paramagnetic Fe(III) phases, likely Fh, and nGt	6.1	0.37	0.51	-	0.24	1.57
	Fe(III)-S2	Magnetite (Tetrahedral)	4.8	0.26	0.04	48.00	1.20	
	Fe(III)Fe(II)-S3	Magnetite (Octahedral)	5.8	0.67	-0.04	45.00	2.00	
	Fe(III)-S1	Likely goethite	83.3	0.38	-0.12	24.52	9.61	
Reacted in ASW	Fe(III)-D1	Paramagnetic Fe(III) phases, likely Fh, Lp and nGt	30.9	0.37	0.58	-	0.15	2.18
	Fe(III)-S1	Likely goethite	69.1	0.37	-0.06	17.30	10.46	

[a]Quadrupole splitting (QS, for doublets) or quadrupole shift (Ɛ, for sextets);
[b]σ, standard deviation of QS (doublet) or H (sextet);
Abbreviations: Fe(III)-D= Fe(III) doublet; Fe(III)-S = Fe(III) sextet; Fe(II)-D = Fe(II) doublet. Fh = ferrihydrite; Lp = lepidocrocite; nGt = nano goethite.

Supplementary Figures

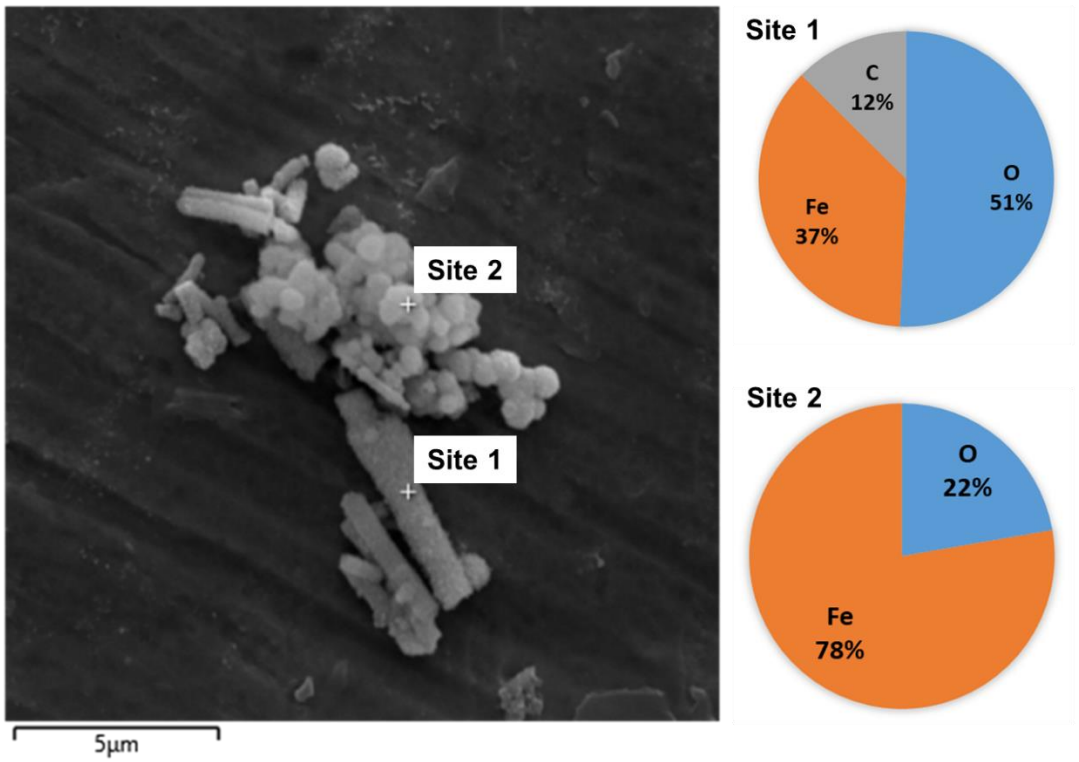

Figure S-1 Main elemental compositions of specific sites on typical structures of the original Fe-rich precipitates based on EDS results. No obvious Si signal (<1%) was identified.

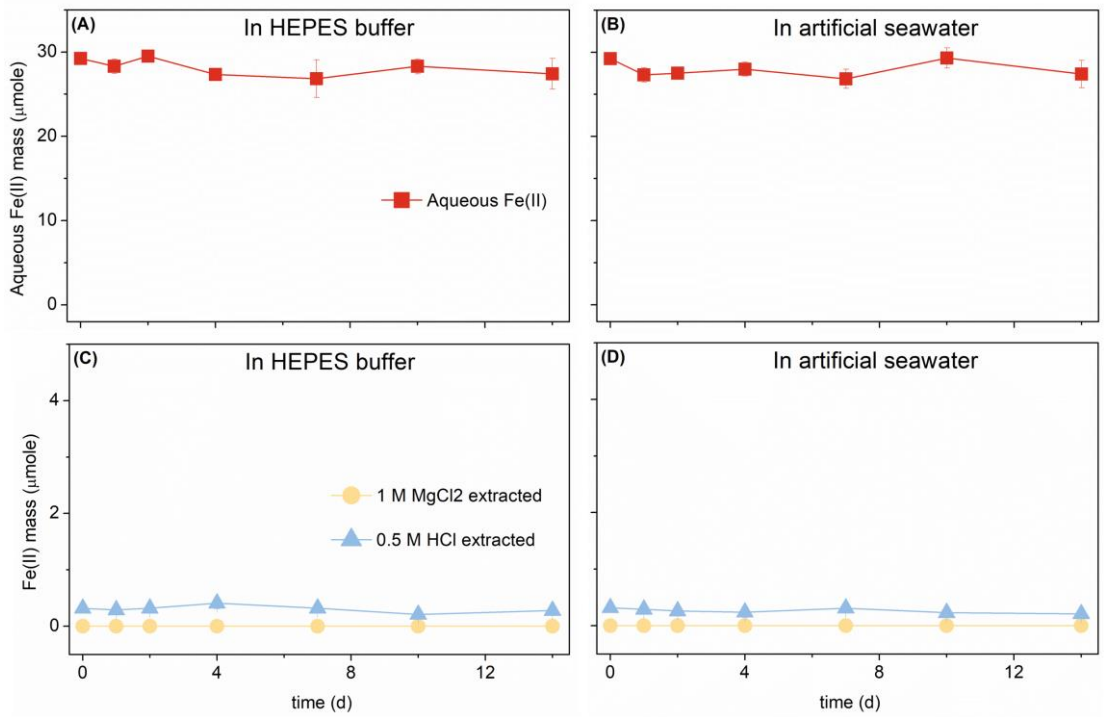

Figure S-2 $Fe(II)_{aq}$ control in (A) HEPES buffer and (B) artificial seawater, as well as the control groups with only the precipitates in (A) HEPES buffer and (B) artificial seawater. Each point represents the mean ± standard deviation of duplicate reactors. Where error bars are not visible, they are smaller than the symbols.

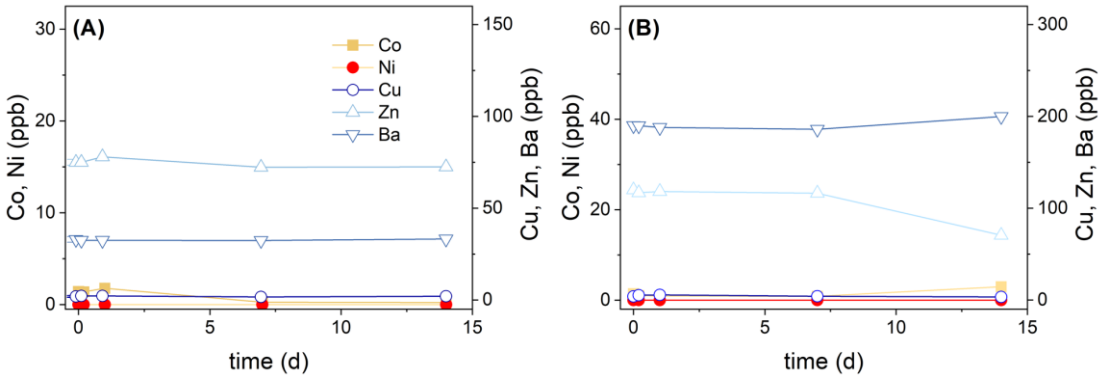

Figure S-3 Aqueous concentrations of Co, Ni (left Y axis) and Cu, Zn, Ba (right Y axis) in the Fe-rich precipitation control (without Fe(II)) in (A) HEPES buffer, and (B) artificial seawater.

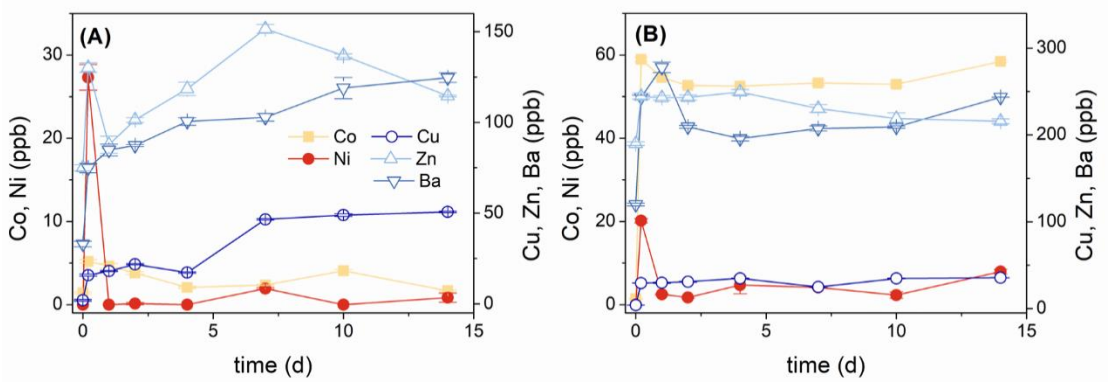

Figure S-4 The concentrations of trace metals in the aqueous phase during the reactions between $Fe(II)_{aq}$ and the precipitates in (A) HEPES buffer, and (B) artificial seawater. Each data point represents the mean ± standard deviation of triplicate reactors.

Supplementary Information References

Vandenberghe, R.E., De Grave, E. (2013) Application of Mössbauer Spectroscopy in Earth Sciences. In: Yoshida, Y., Langouche, G. (Eds.) *Mössbauer Spectroscopy: Tutorial Book*. Springer, Berlin Heidelberg, 91–185. https://doi.org/10.1007/978-3-642-32220-4_3

Viollier, E., Inglett, P., Hunter, K., Roychoudhury, A., Van Cappellen, P. (2000) The ferrozine method revisited: Fe (II)/Fe (III) determination in natural waters. *Applied geochemistry* 15, 785–790. https://doi.org/10.1016/S0883-2927(99)00097-9

Voelz, J.L., Johnson, N.W., Chun, C.L., Arnold, W.A., Penn, R.L. (2019) Quantitative Dissolution of Environmentally Accessible Iron Residing in Iron-Rich Minerals: A Review. *ACS Earth and Space Chemistry* 3, 1371–1392. https://doi.org/10.1021/acsearthspacechem.9b00012

Zhou, Z., Latta, D.E., Noor, N., Thompson, A., Borch, T., Scherer, M.M. (2018) Fe (II)-Catalyzed Transformation of Organic Matter–Ferrihydrite Coprecipitates: A Closer Look Using Fe Isotopes. *Environmental Science & Technology* 52, 11142–11150. https://doi.org/10.1021/acs.est.8b03407